6.2 Large-Eddy Simulation of Wake Vortex Evolution from Roll-Up to Decay

Takashi Misaka, Frank Holzäpfel, Thomas Gerz
Institute of Atmospheric Physics

The development of an aircraft wake vortex from the roll-up until vortex decay is studied. An aircraft model and the surrounding flow field obtained from high-fidelity Reynolds-averaged Navier-Stokes simulation are swept through a ground-fixed computational domain to initialize the wake. After the wake initialization, the large-eddy simulation of the vortical wake is performed until vortex decay. The methodology is tested with the NACA0012 wing and applied to the DLR-F6 wing-body model. The roll-up process of the vorticity sheet from a main wing and the merge of an inboard wing vortex into the wingtip vortex are simulated. Vortex parameters such as the averaged circulation, vortex core radius and vortex separation are also evaluated. The growth rate of the vortex core radius is relatively small during the roll-up where the fine mesh resolution in the LES is required to capture the tiny vortex core in the RANS simulation. A high-lift configuration of a landing large transport aircraft was also studied where the wingtip vortices merge with the co-rotating and stronger outboard flap vortices.

Introduction

Wake vortices generated by a flying aircraft pose a potential risk for following aircraft due to the strong and coherent vortical flow structure [1]. In addition, condensation trails (contrails) originated from the interaction of jet exhaust, wake vortices and the environmental atmosphere may trigger the formation of cirrus clouds (contrail cirrus) which have influence on the climate [2,3]. Wake vortex is related to a broad scale of flows. Flows around aircraft's main wing, fuselage, slat, flap, jet engine and tail plane, and their interactions may affect the generation of wake vortex in particular in a high-lift condition [4]. On the other hand, contrails generated by cruising aircraft spread several tens kilometers.

The evolution of an aircraft wake can be divided into several phases, for example, (1) roll-up phase, (2) vortex phase, and (3) dissipation phase [1]. Although numerical simulation is one of the effective approaches to tackle this problem, the applicable flow scale of a numerical simulation code is usually limited to each of those regimes. High-fidelity Reynolds-averaged Navier-Stokes (RANS) simulations can handle flows around aircraft and subsequent roll-up process of wake vortex in the jet regime [5]. In addition, experimental measurements of near field wake evolutions have been conducted [4,6]. On the other hand, the dynamics of rolled-up wake vortex in the vortex and dissipation regimes has been studied mainly by large-eddy simulation (LES) or direct numerical simulation (DNS). In these researches, detailed temporal evolution of a vortex pair with a longitudinally constant velocity profile is investigated, where short-wave (elliptic) instability and Crow instability may develop. In addition, various atmospheric conditions of turbulence, stability and wind shear are considered to assess the effect of these factors on wake vortex evolution and decay [7-9]. The LES of wake vortex in the late dissipation and diffusion regimes is performed along with microphysical processes of contrails in Ref. [10].

The present study aims to develop a methodology which enables to simulate the wake vortex evolution from the generation until vortex decay, i.e., from the roll-up phase to the end of the vortex phase. We investigate the evolution of vortex parameters such as the averaged circulation, vortex core radius and vortex separation from the wake roll-up until vortex decay. By sweeping a local and stationary flow field obtained around the wing and fuselage of an aircraft with high-fidelity RANS through the LES domain to initialize the wake, it is possible to simulate the entire life cycle of a wake vortex system from realistic wake roll-up processes. The temporal integration of wake vortex until vortex decay is straightforward except for the treatment of longitudinal boundary conditions. Here we consider a simple NACA0012 wing for the numerical tests of the approach. Then the DLR-F6 model in a cruise condition is investigated with and without employing an ambient turbulence field. The roll-up process and subsequent wake evolution

of a large transport aircraft case in high-lift configuration from the AWIATOR project are also simulated. The study, bridging the gap between the roll-up and the vortex phases, shall provide more realistic insights into the aircraft wake vortex evolution expressed in terms of vortex circulation and vortex core radius. It also allows investigating the entrainment of jet exhaust by considering tracers, which might be useful for detailed contrail modeling studies.

Methods

Flow Solver

In this study, the incompressible Navier-Stokes code MGLET is employed for LES [11]. An equation for potential temperature is also solved to take into account buoyancy effects employing Boussinesq approximation. The equations are discretized by a finite-volume approach with the fourth-order finite-volume compact scheme [12]. Lagrangian dynamic model is employed for a turbulence closure [13]. The third-order Runge-Kutta method is used for time integration [14].

Wake Initialization Using RANS Flow Field

The present approach which is schematically shown in Figure 1 could be a numerical realization of the catapult wind tunnel [15]. The numerical approach has several advantages for investigating an aircraft wake. The decay of a vortex pair strongly depends on environmental conditions such as ambient turbulence, temperature stratification and wind shear. Therefore the control of these conditions is crucially important to assess the influence of the ambient conditions on vortex decay. Unlike the consideration of realistic inflow conditions in an aircraft fixed LES domain, the generation of controlled turbulence fields in the ground fixed LES domain is straightforward. The other reason is that the present approach does not need a long computational domain in the flight direction for obtaining longer vortex age compared to an aircraft fixed LES domain.

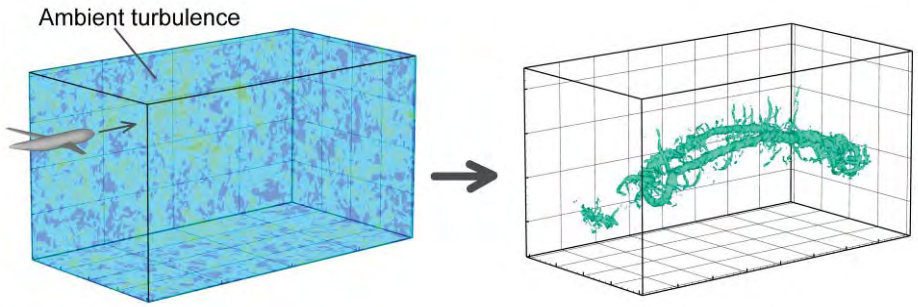

Figure 1. Schematic of the approach, (a) wake initialization, (b) wake evolution until vortex decay.

An aircraft model and the surrounding stationary flow field obtained from a high-fidelity RANS simulation are swept through a ground fixed LES domain to initialize the aircraft's wake [16]. The RANS flow field is added as a forcing term to the Navier-Stokes equations in the LES. Similar approach might be referred to as the fortified solution algorithm (FSA) [17] or a nudging technique used in data assimilation [18]. The resulting velocity field is represented by the weighting sum of RANS velocity field $\mathbf{V}_{RANS}$ and LES velocity field $\mathbf{V}_{LES}$,

$$\mathbf{V} = f(y,\alpha,\beta)\,\mathbf{V}_{LES} + \left[1 - f(y,\alpha,\beta)\right]\mathbf{V}_{RANS}\,. \tag{1}$$

The weighting function $f(y,\alpha,\beta)$ could be a smooth function of the wall-distance y or of other physical quantities such as velocity magnitude. Figure 2 schematically shows the combination of RANS and LES flow fields. Here, we employ the following function of wall-distance to realize smooth transition between the flow fields,

$$f(y,\alpha,\beta)=\frac{1}{2}\left[\tanh\left[\alpha\left(\frac{y}{\beta}-\frac{\beta}{y}\right)\right]+1.0\right], \quad (2)$$

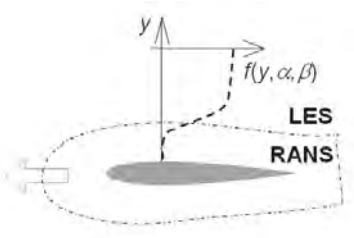

Figure 2. Schematic of the present approach for combining RANS and LES.

where the constants α and β represent the slope of the transition and the wall-distance where solutions of RANS and LES are equality weighted, respectively. These constants can be determined by trial and error, as well as by optimization techniques.

The mapping of the RANS flow field onto the Cartesian LES mesh is performed by a linear interpolation only once before the wake initialization. An additional computer memory is prepared to store the mapped RANS flow field, however, the additional computational cost for the forcing term is minimal. The forward movement of an aircraft is represented by simply shifting the mapped flow field for a certain mesh spacing, which is also possible for a decomposed LES domain if the increments of the advancement is smaller than the halo region of the domain decomposition for parallel computation.

Reproduction of eddy viscosity

Since we only use a RANS velocity field to initialize the wake, the eddy viscosity in the LES domain appears to be low compared to that in the original RANS flow field. Therefore it is required to reproduce velocity fluctuations modelled in the RANS flow field. It is pointed out that the correct representation of eddy viscosity in the wake is important to simulate the wake evolution [19]. Most crude but still useful representation of such velocity fluctuations may be white noise. Here we add white noise to the RANS flow field in the region of RANS-LES transition so that the time-averaged LES eddy viscosity matches to the RANS eddy viscosity in the wake. The magnitude of the fluctuations is modified by the proportional-integral (PI) controller during the advancement of the model through the LES domain.

$$\mathbf{V}'_{\mathrm{RANS}}=\mathbf{V}_{\mathrm{RANS}}+K\mathbf{V}_{\mathrm{WN}}, \quad (3)$$

$$K=a_1(\mu_{t,\mathrm{RANS}}-\overline{\mu}_{t,\mathrm{LES}})+a_2\int(\mu_{t,\mathrm{RANS}}-\overline{\mu}_{t,\mathrm{LES}})dt, \quad (4)$$

where $\mathbf{V}_{\mathrm{WN}}$ is a white noise field and K is a gain to control the magnitude of the velocity fluctuations. The gain is defined by the difference between the RANS eddy viscosity $\mu_{t,\mathrm{RANS}}$ and the time-averaged LES eddy viscosity $\overline{\mu}_{t,\mathrm{LES}}$. These eddy viscosities for calculating the gain are integrated in the wake region with the weighting of the RANS eddy viscosity. The magnitude of the added white noise fluctuation is also weighted locally using the RANS eddy viscosity. The constants a_1 and a_2 are set according to the convergence of the gain and numerical stability but the results are not too sensitive to these values.

Optimization of the RANS-LES Interface

In the above formulation, RANS and LES solutions are switched using a certain threshold, i.e., a constant distance from the body surface (wall-distance). On the other hand, it is possible to define the distance locally by using optimization techniques with respect to an appropriate cost function. We tested a cost function defined by the difference of axial vorticity magnitudes between two longitudinal positions,

$$J(\alpha,\beta)=\frac{1}{2}(\omega_{x2}-\omega_{x1})^2, \quad (5)$$

$$\omega_{x1}=\omega_x\big|_{x=x1},\ \omega_{x2}=\omega_x\big|_{x=x2},\ \omega_x=(\nabla\times\mathbf{V})_x. \quad (6)$$

This cost function is evaluated locally, i.e., the upstream axial vorticity magnitude ω_{x2} at x_2 and the downstream axial vorticity ω_{x1} at x_1 are evaluated at each (x,y,z) position in the transition region. The cost function is minimized by gradient-based optimization methods. The gradients of the cost function are obtained as follows,

$$\nabla_\alpha J(\alpha,\beta) = \left(\frac{\partial f}{\partial \alpha}\right)^T (\delta\omega_{x2} - \delta\omega_{x1})(\omega_{x2} - \omega_{x1}), \tag{7}$$

$$\nabla_\beta J(\alpha,\beta) = \left(\frac{\partial f}{\partial \beta}\right)^T (\delta\omega_{x2} - \delta\omega_{x1})(\omega_{x2} - \omega_{x1}), \tag{8}$$

$$\delta\omega_{x1} = \delta\omega_x\big|_{x=x1},\ \delta\omega_{x2} = \delta\omega_x\big|_{x=x2},\ \delta\omega_x = \left[\nabla\times\left(\mathbf{V}_{\mathrm{LES}} - \mathbf{V}_{\mathrm{RANS}}\right)\right]_x. \tag{9}$$

Here the derivations of the switching function *f* can be obtained analytically from Eq. (2). Using this gradient, the search direction is defined based on the conjugate gradient method. Smoothing of the parameters α and β is required to achieve a sufficiently smooth transition between the flow fields.

Results and Discussion

The NACA0012 Wing

Numerical tests of the present approach are performed by using a simple rectangular wing. The wing has NACA0012 cross-section and a rounded wingtip. Inflow velocity of 52 m/s and angle of attack of 10 degrees are considered. Wind tunnel test of this configuration was conducted by Chow *et al.* [20] and numerical studies followed that configuration to investigate higher-order schemes, turbulence models and so on [21]. Figure 3 shows a computational domain for RANS to obtain the near flow field and a longer domain for sweeping the RANS flow field based on the present approach. In Figure 3, the velocity magnitude and the computational mesh are shown in the RANS domain. In addition, the pressure on the root-side wall and the iso-surface of the vorticity magnitude are shown in the LES domain. For the RANS simulation, an incompressible flow solver from a free CFD software package, OpenFOAM, is used [22].

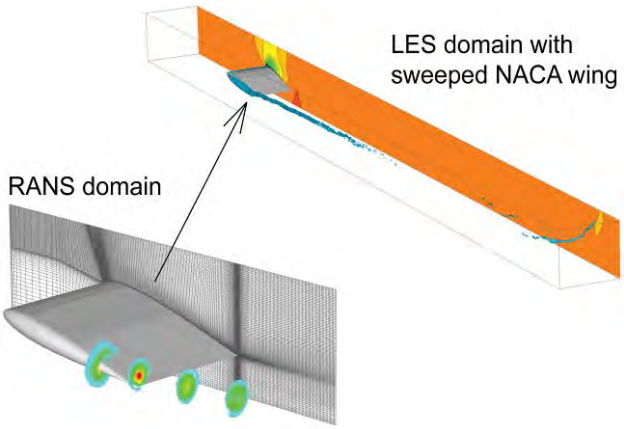

Figure 3. Computational domains for RANS simulation and for sweeping the RANS flow field.

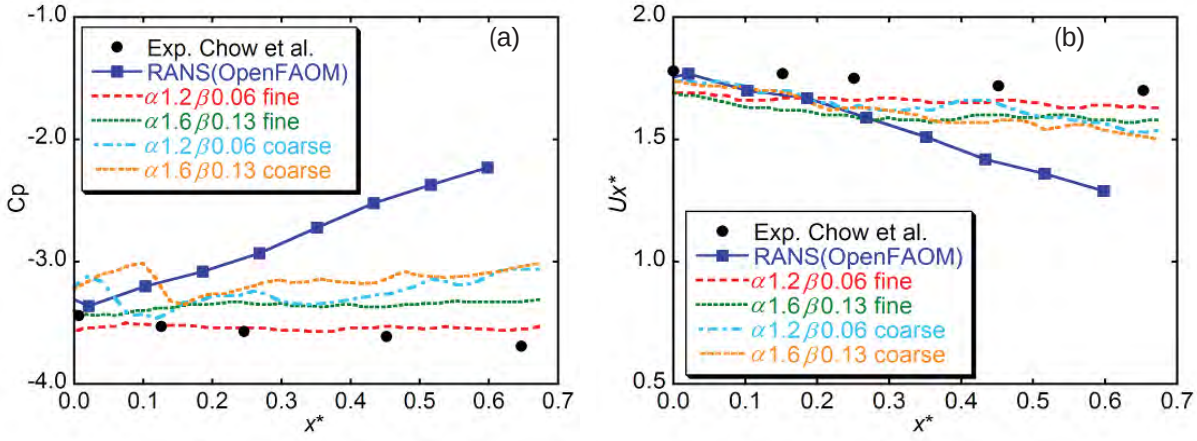

Figure 4. Vortex parameters along vortex centerline (a) pressure coefficient, (b) axial velocity.

The experimental and RANS results as well as the results from the present approach with two sets of parameters (α = 1.2, β = 0.06), (α = 1.6, β = 0.13) for two different mesh resolutions (dx^* = 0.005, 0.01) are compared in Figure 4. Figure 4(a) shows the pressure coefficient along the vortex centerline where the origin of x^* is set to the trailing edge of the wing and it is normalized by a wing chord length. The

pressure in the vortex centre increases quickly in the RANS case which indicates an early diffusion of the vortex in the present RANS simulation. This is mainly due to the coarser grid resolution and the low order numerical scheme compared to other RANS simulations [21]. On the other hand, the present approach uses only the RANS near field data around the body, therefore, it shows better results compared to the RANS case. The case with the parameter set (α = 1.2, β = 0.06) and fine mesh appears closest to the experiment. In the coarse mesh cases, there are kinks of the pressure coefficient near the switching wall-distances of β = 0.06 and 0.13. Figure 4(b) shows the axial velocity along the vortex centreline. All the cases from the present approach appear to be low compared to the experiment. Unlike the pressure coefficient, there is no kink near the switching wall-distance in the coarse mesh cases.

Figure 5(a) and (b) show the switching wall-distance of the RANS and LES flow fields by green transparent surfaces before and after the optimization, respectively. The vorticity iso-surface in red shows the wingtip vortex. The switching distance is decreased near the wingtip vortex in Figure 5(b). Figure 5(c) shows the result with optimization of the switching wall-distance based on the cost function in Eq. (5). The kink of the pressure coefficient in coarse mesh cases is alleviated by modifying the switching wall-distance locally.

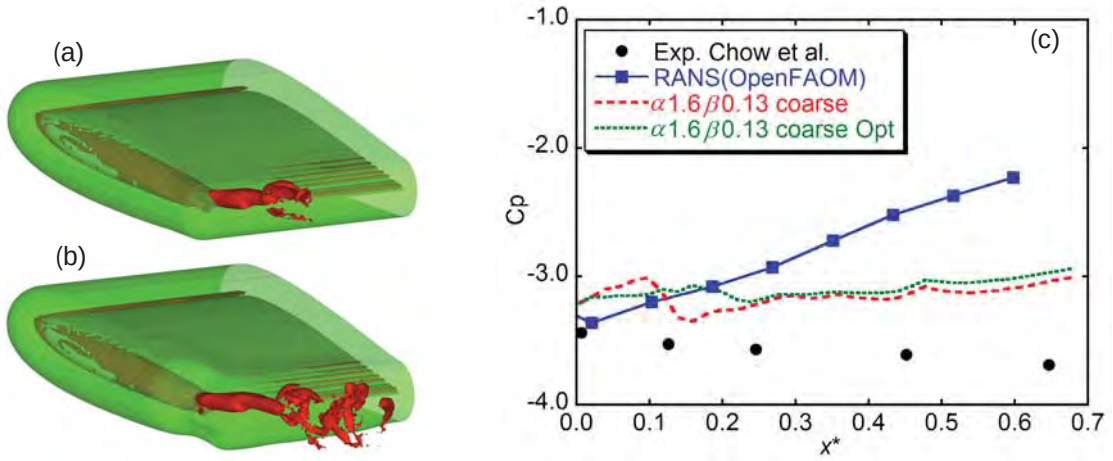

Figure 5. Iso-surfaces of the threshold β (green transparent) and vorticity magnitude (red) for (a) constant β = 0.13, (b) locally optimized β using the cost function Eq. (5), and (c) pressure coefficient with and without optimization based on the cost function.

The DLR-F6 Model

As for a more realistic case, we employed the DLR-F6 wing-body model in clean (low-lift) configuration to initialize the wake. The RANS solution is obtained by the DLR TAU-code with hybrid unstructured mesh, where the number of mesh points is approximately 8.5 million [23]. The flow conditions of Mach number M=0.75 and Reynolds number Re=5.0x10^6 are considered. Note that the RANS flow field used here is not prepared for wake investigations but for the accurate prediction of aerodynamic forces such as lift and drag coefficients. Therefore, the mesh resolution behind the trailing edge is not enough to sharply capture wingtip vortices, which is a similar situation as in the previous NACA0012 wing case. To normalize the quantities, we use the reference values, assuming an elliptic load distribution of the wing,

$$\Gamma_0 = \frac{2C_L U b}{\pi \Lambda}, \quad b_0 = \frac{\pi}{4} b, \quad w_0 = \frac{\Gamma_0}{2\pi b_0}, \quad t_0 = \frac{b_0}{w_0}, \tag{8}$$

where C_L, U, b, and Λ represent a lift coefficient C_L = 0.5, uniform flow speed U = 270 m/s, wingspan b = 1.172 m, and wing aspect ratio Λ = 9.5, respectively. These values are from the experimental conditions. Using these numbers the reference values for the normalization become Γ_0 = 10.5 m^2/s, b_0 = 0.92 m, w_0 = 1.8 m/s, and t_0 = 0.5 s, respectively.

Figure 6 shows the axial vorticity distribution on a plane at the distance of x^* = 5.3 from the trailing edge of the wingtip, which corresponds to t^* = 0.03 after the passage of the wingtip through the plane. The peak vorticity is labeled at the vortices. Here the mesh resolution and the switching wall-distance are varied. Comparing the three different mesh resolutions shown in Figures 6(a), (b), and (e), it is evident that the finest mesh clearly preserves the vorticity distribution during roll-up the best. Especially, the roll-up of a vorticity sheet from the main wing with many details is clearly seen in Figure 6(e). The vorticity peaks are also maxima in this finest mesh case. The influence of the switching wall-distance is observed from Figures 6 (b), (c), and (d), where the result with β = 0.07 in Figure 6(d) is close to the result of the finest mesh with the same switching wall-distance β = 0.07.

The dependence of the results on the switching wall-distance is reduced by using a RANS flow field with mesh refinement in the wake region [5]. The other possibility to alleviate the dependency is to use the optimization of the switching wall-distance locally as shown in the previous NACA0012 case. The optimization of the switching wall-distance is effective to obtain a sharp wake while realizing smooth transition of RANS-LES flow fields in other regions.

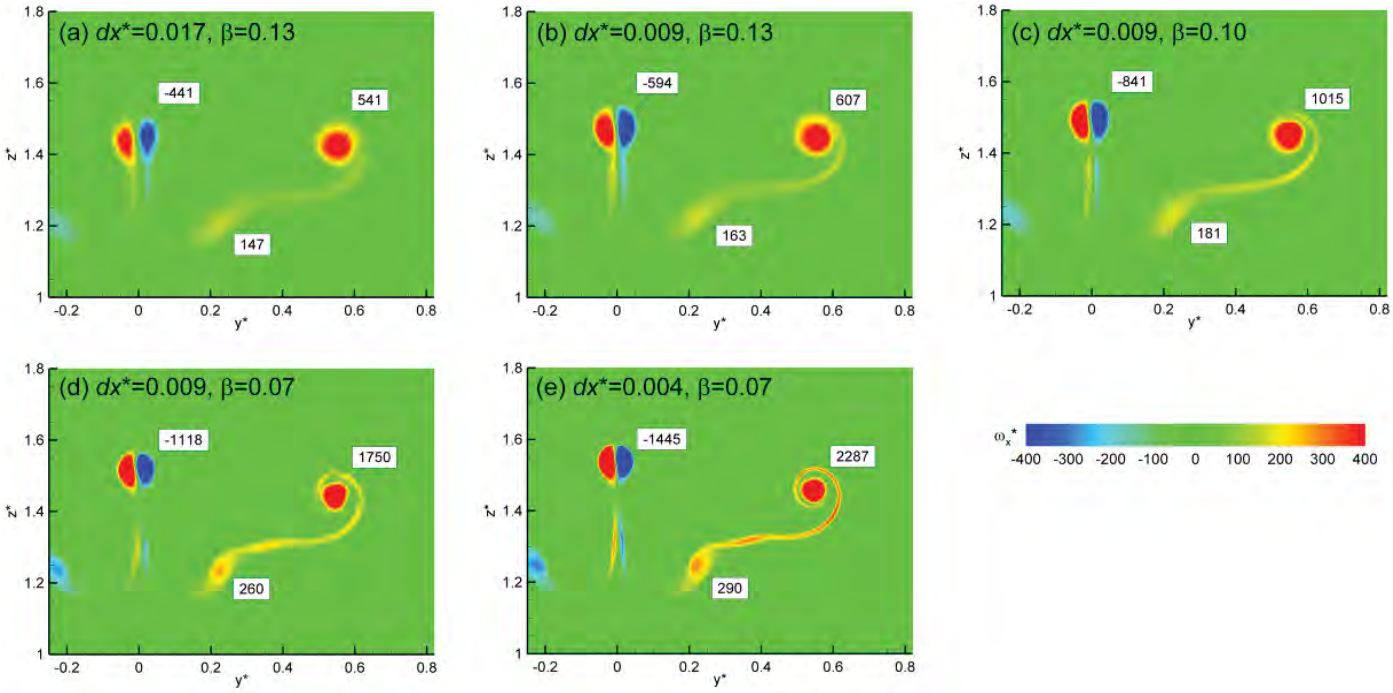

Figure 6. Vorticity distributions at x^* = 5.3 during the roll-up of DLR-F6 model's wake.

For the following analysis of the F6 model wake, the parameters used are dx*= 0.009 and β = 0.1; the optimization technique is not applied. Figure 7 shows the wake roll-up and the subsequent evolution of a vortex pair. Here the ambient turbulence is characterized by eddy dissipation rate of ε^* = 0.01. Temperature stratification is not considered. The flow field is visualized by two levels of iso-vorticity surfaces (red: $|\omega^*|$ = 250, blue transparent: $|\omega^*|$ = 65). The midpoint of the visualized wake in flight direction corresponds to the labelled position and time. The wingtip vortices and the fuselage wake have large vorticity magnitudes in the beginning. The jet-like fuselage wake decays relatively quickly while the wingtip vortices preserve large vorticity. The decayed fuselage wake and the vorticity from inboard wing (see also Figure 6) wrap around the wingtip vortices adding disturbances around them. A stable vortex pair appears between t* = 1 and 2 (cf. Figure 7 f and g). At t^* = 8.8, the vortex pair is highly disturbed and almost decayed.

Note that there is a difference of the vortex age between the both sides of the domain in flight direction after the wake initialization. Here the flow field is inverted slicewise to close the domain periodically. The resulting LES domain is two times larger than the original one, i.e., two times larger computational cost,

but it is possible to apply periodic boundary conditions also for the longitudinal boundaries. The inverted part of the domain is not shown in Figure 7, where it is confirmed that the influence of the boundary treatment is not noticeable.

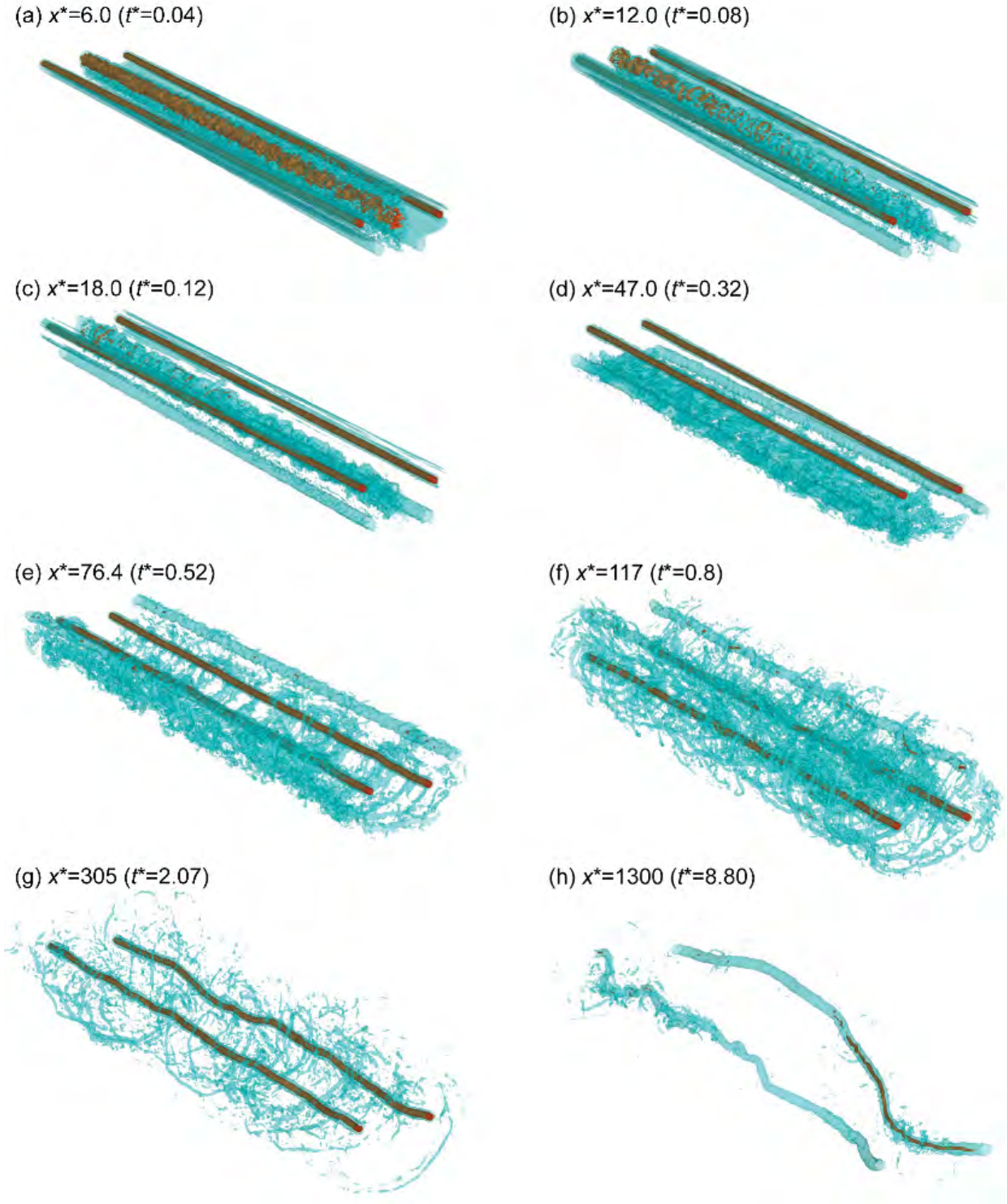

Figure 7. Temporal evolution of the vorticity distribution (red: $|\omega^*| = 250$, blue transparent: $|\omega^*| = 65$) of the wake behind the DLR-F6 model.

Figure 8(a) shows the circulation averaged between the non-dimensional vortex core radii of 0.106 to 0.318, which corresponds to the circulation averaged between core radii of 5 to 15 m, denoted as $\Gamma^*_{5\text{-}15}$,

used in real-scale field measurements. Here the $\Gamma^*_{5\text{-}15}$ is averaged along vortex centerlines in the domain. The plot shows ε^* = 0.01, N^* = 0.0 and ε^* = 0.01, N^* = 0.35 cases as well as the case using Lamb-Oseen vortex model as in the conventioal LES of a vortex pair. The horizontal axes denote the distance from the wingtip (bottom) and the time (top). The start time of Lamb-Oseen model case is shifted because the Lamb-Oseen model represents a fully rolled-up vortex pair. There is a peak of the averaged circulation during the roll-up, and the initial decay rate is larger than in the Lamb-Oseen case. The circulation peak corresponds to the completion of the roll-up process (see also Figure 7), whereas the stronger decay rate might reflect the effect of the entrainment of the turbulence from the fuselage wake. It is also confirmed that the stable stratification effectively enhances circulation decay.

Figure 8 (b) shows the evolution of the vortex separation. It exhibits a local minimum followed by a local maximum value during the roll-up process. After about t^* = 2, the neutrally and stratified cases differ, the vortex spacing increases monotonously in the former case, whereas it stays first constant and then decreases slightly in the latter case. A similar evolution is noticed for the stratified Lamb-Oseen case. Figure 8 (c) shows the evolution of vortex core radii. The initial value of the core radius in the Lamb-Oseen case is set to 0.045. In all cases the vortex core radii evolve identically for six time units or about 900 vortex spacings behind the aircraft. Then the stratified cases show an abrupt increase; the neutral case follows about 2 t_0 later. The peak tangential velocities shown in Figure 8 (d) rapidly drop after the roll-up at t^* = 1, while the root-mean-square (RMS) velocity fluctuations along the vortex increase sharply. These observations corroborate the effect of the entrainment of fuselage turbulence into the main vortex pair and the larger decay rate of the averaged circulation in the early vortex phase (Figure 8a).

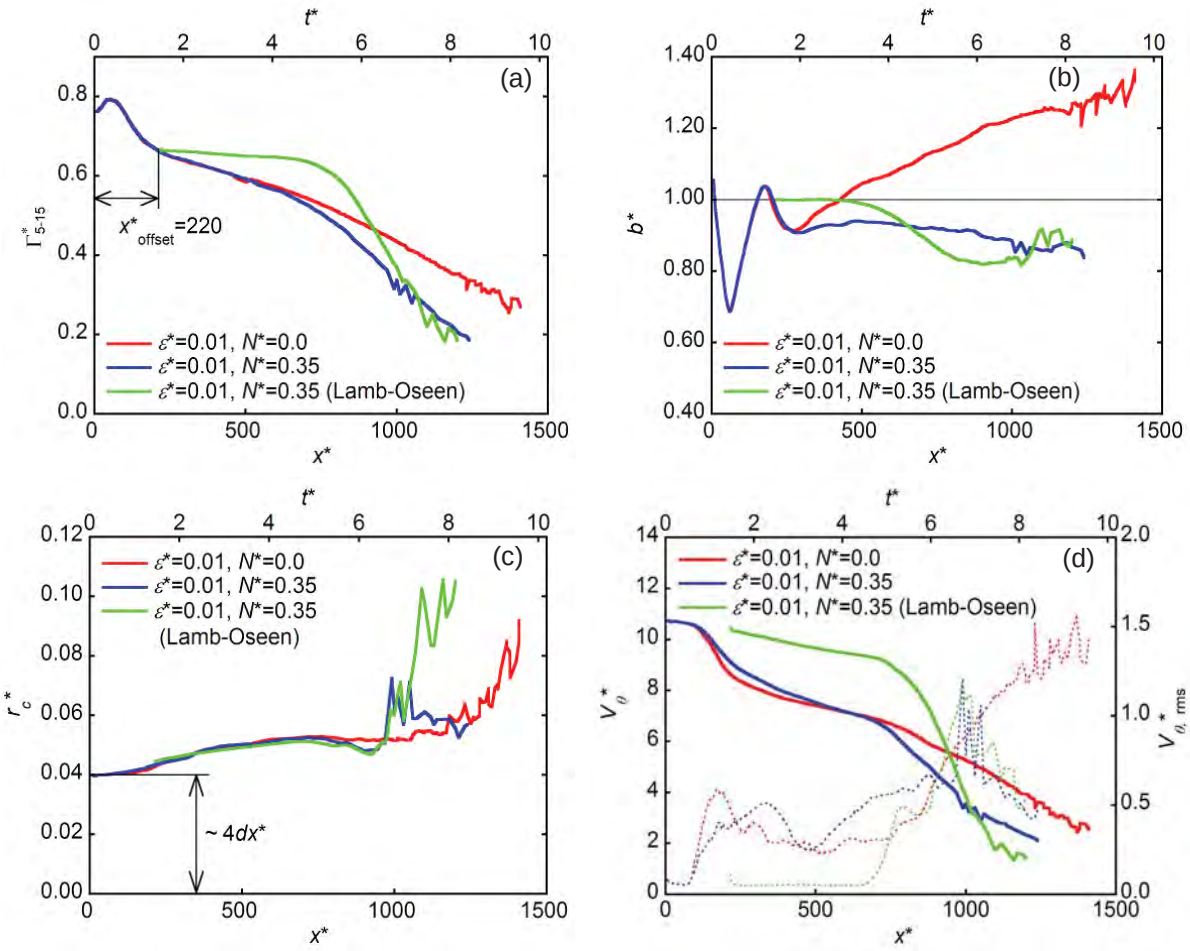

Figure 8. Temporal evolutions of (a) averaged circulation, (b) vortex separation, (c) vortex core radius, and (d) peak tangential velocity generated by the DLR-F6 model.

The AWIATOR case of a large transport aircraft

Another realistic configuration is a large transport aircraft model used in ONERA's catapult tunnel during the European AWIATOR project. The 1/27 scaled model has span width of 2.236 m. The experiment conditions are Re = 5.2×10^5, U_∞=25 m/s, and C_L = 1.4. Applying similar normalization as the previous DLR-F6 case, we have Γ_0 = 5.36 m^2/s, b_0 = 1.756 m, w_0 = 0.49 m/s, and t_0 = 2.0 s. The RANS solution is obtained by the DLR TAU-code with the adaptive mesh refinement for wingtip and flap vortices as well as for fuselage wake. The RANS/LES coupling was achieved with the setting dx*= 0.009 and β = 0.07; the optimization technique is not applied.

Figure 9 shows the evolution of vorticity distribution on a ground fixed vertical plane from t^* = 0.32 until 1.631. In this high-lift configuration, the vortices from the deployed outboard flap are stronger than wingtip vortices. As a result, the wingtip vortex rotates around the outboard flap vortex and merges to the outboard flap vortex at t^* = 0.742. The vorticity shed by the fuselage is relatively large in the beginning, however, the magnitude decreases quickly due to mutal cancellation across the symmetry line. The vorticity shed by the through-flow nacelles also decays quickly. Similar to the DLR-F6 case it takes about one time unit to complete the roll-up process.

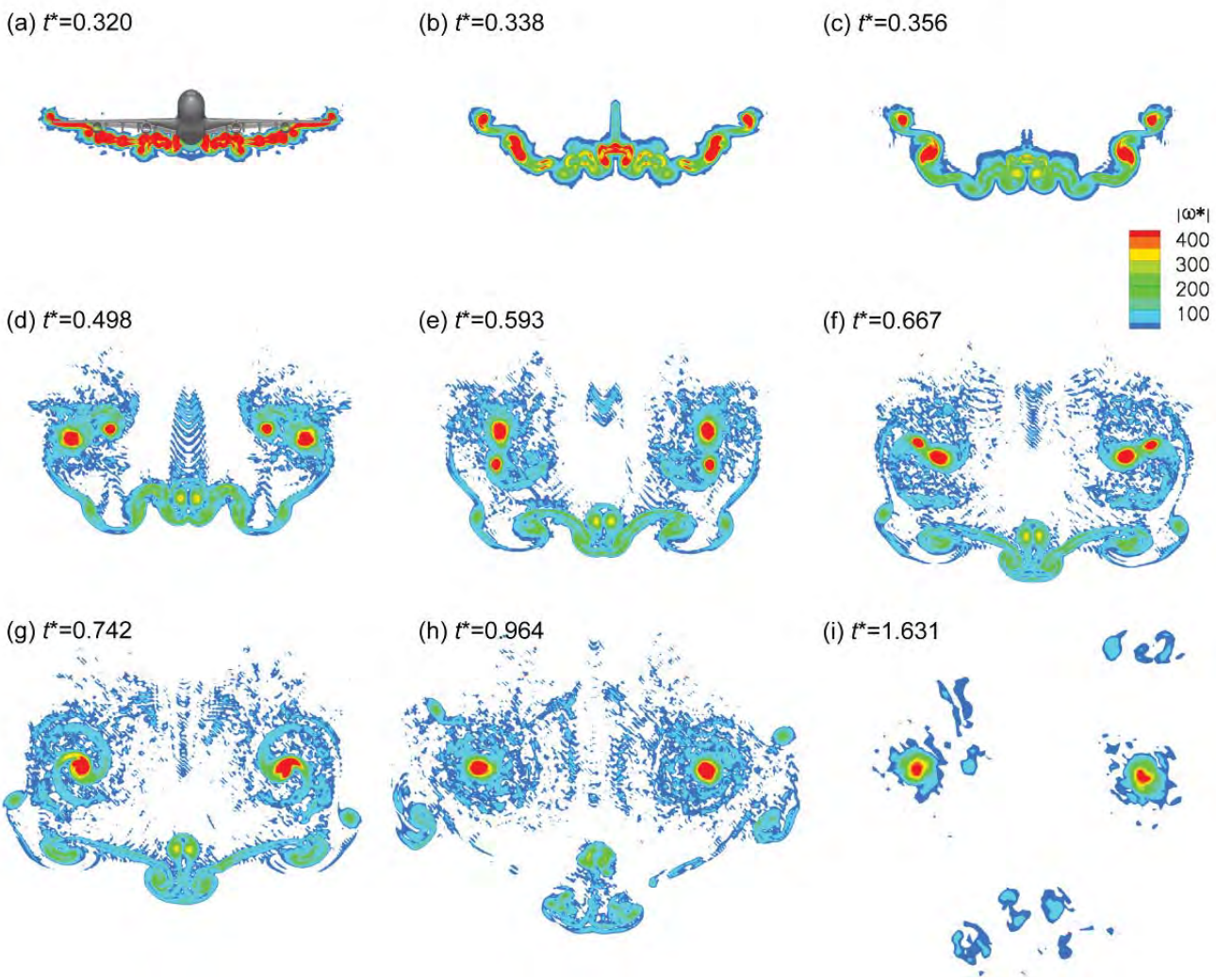

Figure 9. Evolution of vorticity distribution during roll-up of the wake of the large transport aircraft model

Conclusions

LES of wake vortex evolution from its generation until vortex decay is performed by combining RANS and LES flow fields. The RANS flow field is employed in the LES as a forcing term sweeping through the ground-fixed LES domain. An eddy viscosity initialization to match the time-averaged LES and RANS eddy viscosities, as well as an optimization technique to obtain the best switching wall-distance in the RANS/LES coupling are proposed.

The methodology is tested using the NACA0012 wing. The present approach achieves comparable results with the experiment by using the RANS flow field very near around wings and fuselage and LES elsewhere. This way the wingtip vortex properties observed in the experiment are well reproduced. The RANS alone is too diffusive to reproduce the experimental results downstream the trailing edge.

Further, the roll-up process of the wake initialized by the DLR-F6 model in low-lift configuration is simulated. The roll-up processes of the vorticity sheet emanating from the wing and tight vortices from the wingtip are simulated. A stable vortex pair appears after this. The growth of the vortex core radius is small especially after the roll-up, where the vortex core radius still depends on the mesh resolution considered here. Finally, the methodology is applied to a model of a large transport aircraft. In this high-lift case, the vortices generated from the outboard flaps are stronger than the wingtip vortices. Therefore, the wingtip vortices wrap around the outboard flap vortices, merging occurs at $t^* = 0.74$. The roll-up process is completed about one time unit after “fly-by” as in the clean low-lift case of the F6 model.

Acknowledgements

We would like to thank Olaf Brodersen, Niko Schade and Bernhard Eisfeld (Institut für Aerodynamik und Strömungstechnik) for providing the RANS data of the DLR-F6 model and Stefan Melber (Institut für Aerodynamik und Strömungstechnik) for the RANS data of the large transport aircraft model. We also thank Prof. Michael Manhart and Dr. Florian Schwertfirm for the provision of the original version of LES code MGLET. Computer time provided by Leibniz-Rechenzentrum (LRZ) is greatly acknowledged. We thank Airbus for the allowance to use the near field wake data of the large transport aircraft model for our computations.

References

[1] Gerz, T., Holzäpfel, F., and Darracq, D., “Commercial Aircraft Wake Vortices,” Progress in Aerospace Science, Vol. 38 (2002), pp. 181-208.

[2] Minnis, P., Young, D. F., Ngyuen, L., Garber, D. P., Smith Jr., W. L., and Palikonda, R. “Transformation of Contrails into Cirrus during SUCCESS,” Geophysical Research Letters, Vol. 25 (1998), pp. 1157-1160.

[3] Schumann, U., Graf, K., and Mannstein, H., “Potential to Reduce the Climate Impact of Aviation by Flight Level Change,” AIAA Paper 2011-3376, 2011.

[4] Breitsamter, C., “Wake vortex Characteristics of Transport Aircraft,” Progress in Aerospace Science, Vol. 47 (2011), pp. 89-134.

[5] Stumpf, E., “Study of Four-Vortex Aircraft Wakes and Layout Corresponding Aircraft configurations,” Journal of Aircraft, Vol. 42 (2005), pp. 722-730.

[6] Rossow, V. J., “Lift-Generated Vortex Wakes of Subsonic Transport Aircraft,” Progress in Aerospace Science, Vol. 35 (1999), pp. 507-660.

[7] Holzäpfel, F., Hofbauer, T., Darracq, D., Moet, H., Garnier, F., and Gago, C. F., “Analysis of Wake Vortex Decay Mechanisms in the Atmosphere,” Aerospace Science and Technology, Vol. 7 (2003), pp. 263-275.

[8] Holzäpfel, F., Gerz, T., Frech, M., and Dörnbrack, A., “Wake Vortex in Convective Boundary Layer and Their Influence on Following Aircraft,” Journal of Aircraft, Vol. 37 (2000), pp. 1001-1007.

[9] Proctor, F. H., Hamilton, D. W., and Han, J., “Wake Vortex Transport and Decay in Gound Effect: Vortex Linking with the Ground,” AIAA Paper 2000-757 (2000).

[10] Unterstrasser, S., Sölch, I., “Study of Contrail Microphysics in the Vortex Phase with a Lagrangian Particle Tracking Model,” Atmospheric Chemistry and Physics, Vol. 10 (2010), pp. 3922-.

[11] Manhart, M., “A Zonal Grid Algorithm for DNS of Turbulent Boundary Layer,” Computer and Fluids, 33 (2004), pp. 435-461.

[12] Hokpunna, A., and Manhart, M., “Compact Fourth-order Finite Volume Method for Numerical Solutions of Navier-Stokes Equations on Staggered Grids,” Journal of Computational Physics, Vol. 229 (2010), pp. 7545-7570.

[13] Meneveau, C., Lund, T. S., and Cabot, W. H., “A Lagrangian Dynamic Subgrid-scale Model of Turbulence,” Journal of Fluid Mechanics, Vol. 319 (1996), pp. 353-385.

[14] Williamson, J. H., “Low-storage Runge-Kutta Schemes,” Journal of Computational Physics, Vol. 35, No. 48, 1980, pp. 48-56.

[15] Coton, P., “Study of Environment Effects by Means of Scale Model Flight Test in a Laboratory,” 21st ICAS Congress, ICAS-98-391, Melbourne, September 1998.

[16] Misaka, T., Holzäpfel, F., Gerz, T., Manhart, M., and Schwertfirm, F., “Large-Eddy Simulation of Wake Vortex Evolution from Roll-Up to Vortex Decay,” AIAA Paper 2011-1003, 2011.

[17] Fujii, K., “Unified Zonal Method Based on the Fortified Solution Algorithm,” Journal of Computational Physics, Vol. 118 (1995), pp. 92-108.

[18] Kalnay, E., Atmospheric Modeling, Data Assimilation and Predictability, Cambridge University Press, 2003.

[19] Czech, M. J., Miller, G. D., Crouch, J. D., and Strelets, M., “Near-field Evolution of Trailing Vortices Behind Aircraft with Flaps Deployed,” AIAA Paper 2004-2149, 2004.

[20] Chow, J., Zilliac, G., and Bradshaw, P., “Turbulence Measurements in the Near Field of a Wingtip Vortex,“ NASA TM-110418, 1997.

[21] Dacles-Mariani, J., Zilliac G., Chow, J., and Bradshaw, P., “Numerical/Experimental Study of a Wingtip Vortex in the Near Field,“ AIAA Journal, 33 (1995), pp. 1561-1568.

[22] http://www.openfoam.com/

[23] Brodersen, O., Eisfeld, B., Raddatz, J., and Frohnapfel, P., “DLR Results from the Third AIAA Computational Fluid Dynamics Drag Prediction Workshop,“ Journal of Aircraft, 45 (2008), pp. 823-836.